Proceedings of the
Annual Stability Conference
Structural Stability Research Council
Atlanta, Georgia, April 21-24, 2026

Residual axial capacity of square hollow tubular columns after lateral impact while under compression loading

Prithvi Sangani[1], Aayush Dua[2], and Anil Agarwal[3]

Abstract

This study examines the residual axial capacity of square hollow tubular columns subjected to lateral impact by a projectile while under compressive loading. Experiments were conducted using a gas gun and barrel setup to launch projectiles. The tested columns measured 200 mm in cross-sectional size, 1800 mm in length, and had an unsupported length of 1500 mm. Special care was taken to make sure that the axial load was maintained during the impact testing. Tests were performed under simply supported conditions and included variations in tube thickness, axial load levels, and projectile type i.e., rigid and deformable projectiles. Both projectile types had the same total weight (26.5 kg) and similar head geometry (139 mm outer diameter hemisphere). The deformable projectile featured a hollow 3 mm-thick head, while the rigid one was solid. All impacts were conducted at a velocity of 20 m/s. Following impact, the columns were subjected to axial compression until failure to evaluate their residual capacities. Strain-rate sensitive finite element models were developed and validated against experimental data, showing good agreement in reproducing impact response and residual axial capacity. Results show that projectile deformability had a pronounced effect on post-impact behavior, with rigid projectiles causing greater reduction in residual axial capacity than deformable projectiles.

1. Introduction

Steel square hollow sections (SHS) are widely used as axially loaded columns in offshore platforms, bridges, industrial facilities, and protective structures due to their high strength-to-weight ratio and compact geometry (Wardenier 2011; Zeinoddini et al., 2002). However, SHS columns are vulnerable to accidental lateral impacts, which often occur while the members are subjected to significant axial compression. Such impacts can induce localized denting and global bending, leading to a substantial reduction in residual axial load-carrying capacity and an increased risk of progressive failure. Prior studies have shown that axial preload, boundary conditions, impact characteristics, and material properties strongly influence impact response and post-impact behavior, with axial compression generally reducing impact resistance and amplifying deformation and instability (Chen et al., 2025; Cui et al., 2023; Li et al., 2019; Sangani et al., 2023, 2024c; a, 2025; Sangani and Agarwal 2024). Although post-impact residual capacity has been studied for hollow and concrete-filled tubular members, most investigations rely on rigid impactors under simplistic boundary conditions, limiting applicability to real structural members under

[1] Research Scholar, Indian Institute of Technology, Hyderabad, India ce20resch13001@iith.ac.in
[2] M.Tech Student, Indian Institute of Technology, Hyderabad, India ce21b25m100001@iith.ac.in
[3] Associate Professor, Indian Institute of Technology, Hyderabad, India anil@ce.iith.ac.in

vehicle-type collisions. Significant gaps remain in understanding the post-impact performance of thin-walled steel tubular columns subjected to deformable impacts, which are known to produce more distributed damage and different energy transfer mechanisms than rigid impactors. Moreover, unintended multiple impacts in drop-weight tests complicate residual capacity assessment. This study addresses these limitations through a combined experimental and numerical investigation of axially preloaded SHS steel columns subjected to lateral impact by both rigid and deformable projectiles of identical mass and velocity, followed by residual axial compression tests. A validated finite element framework is developed to simulate the complete sequence of axial preloading, lateral impact, unloading, and residual axial compression.

2. Test Program

Six YSt 310 steel columns were tested to investigate their as-built and post-impact axial residual strength. Two specimens were tested under monotonic axial compression to establish benchmark axial capacities, while the remaining four were subjected to combined axial preload and lateral impact, followed by post-impact axial compression. The test specimens consisted of SHS with a side length of 200 mm and wall thicknesses of 6 mm (S6) and 8 mm (S8) (Fig. 1(a)). All columns had an overall length of 1800 mm, with an unsupported length of 1500 mm during impact testing. Lateral impact was applied using deformable and rigid projectiles, each having a nominal diameter of 139 mm and a mass of 26.5 kg with hemispherical noses (Fig. 1(b and c)). The deformable projectiles were fabricated from EN8 steel, while the rigid projectile was machined from solid steel.

Tensile coupon tests were conducted in accordance with ASTM E8 (2010) to determine mechanical properties. The coupons were extracted along the rolling direction, and three specimens were tested for each material. The resulting engineering stress-strain responses are shown in Fig. 2, and the average mechanical properties are summarized in Table 1. The test matrix (Table 2) considered the effects of column wall thickness, axial load ratio (R), and projectile type. The axial load ratio (R) is defined as the ratio of the applied axial load to the axial capacity of the corresponding column. All impact tests were conducted at a nominal impact velocity of 20 m/s.

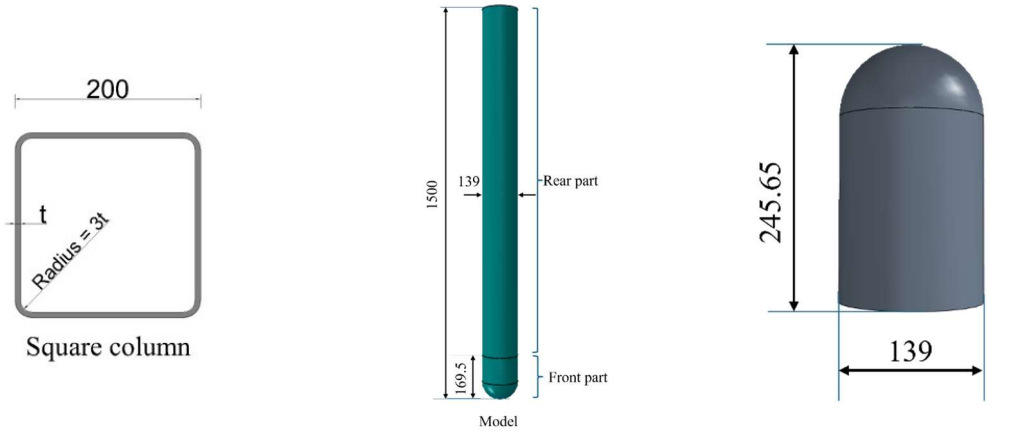

(a) SHS cross-section (b) Deformable projectile (c) Rigid projectile

Figure 1: Geometry details

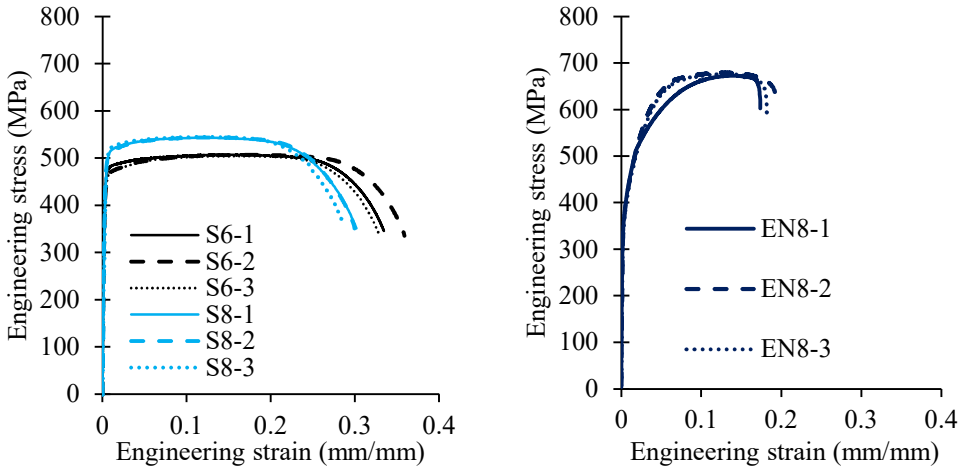

(a) Square columns (YSt 310) (b) Projectile material

Figure 2: Engineering stress-strain plots for column and projectile material

Table 1: Mechanical properties

Specimen	Elastic modulus, E (MPa)	Proof stress, $\sigma_{0.2}$ (MPa)	Ultimate stress, σ_{ult} (MPa)	Fracture strain (ε_f)
S6	200400	442	507	0.341
S8	193600	472	544	0.296
EN8	204100	370	678	0.183

Table 2: Test matrix

	Specimen notation	Column thickness (mm)	Projectile	Axial capacity (kN)	Axial preload (kN)	Axial load ratio (R)	Impact velocity (m/s)
Axial compression tests	S6	5.85	-	1914	-	-	-
	S8	7.67	-	2514	-	-	-
Impact tests	S6-def-0.0	5.85	Steel	1914	0	0.0	19.98
	S6-def-0.2	5.85	Steel	1914	380.6	0.2	20.51
	S8-def-0.2	7.67	Steel	2514	504.6	0.2	20.66
	S6-rigid-0.2	5.85	Rigid	1914	379.2	0.2	20.33

Prior to impact testing, the axial capacities of the columns were determined through monotonic compression tests conducted using a 12,000 kN compression testing machine. Simply supported boundary conditions were simulated by welded end plates fitted with semi-cylindrical rollers. From these tests, the axial capacities were measured to be 1,915 kN and 2, 514 kN for the S6 and S8 columns, respectively.

2.1 Impact tests

Lateral impact tests were performed using a pneumatic gas-gun facility (Fig. 3) developed at IIT Hyderabad. The setup was configured to launch projectiles at a target impact velocity of 20 m/s. During testing, the columns were subjected to an axial preload followed by lateral impact while maintaining simply supported boundary conditions (Fig. 4). To permit free axial translation and rotation while restraining lateral displacement, custom roller-pin end assemblies were employed. These assemblies consisted of a concave-convex steel interface with cylindrical rollers placed between them ensuring proper alignment and efficient load transfer during impact.

A self-reacting disc spring assembly was used to maintain a nearly constant axial force throughout the impact event. The axial preload was applied using a hydraulically controlled jack acting through a calibrated load cell (Fig. 4). Mid-span lateral deformations were measured using linear variable differential transformers (LVDTs) while axial loads were continuously monitored using load cells. High-speed cameras arranged in a stereo configuration were used to capture projectile motion and column deformation. The projectile deceleration obtained from the DIC measurements was multiplied by the projectile mass to compute the impact force-time histories.

The impact force-time histories and projectile displacement histories are presented in Fig. 5(a) and (b), respectively. A summary of the impact test results is provided in Table 3. Preliminary observations from the lateral impact tests indicated that column deformation was predominantly localized, characterized by distinct dent formation at the impact location, while the deformable projectile heads also experienced localized damage. At the cross-sectional level, the impacted face underwent inward bending, accompanied by outward bulging of the adjacent faces. Damage severity was higher for rigid projectile impacts compared to deformable projectile impacts. In the case of deformable projectiles, significant permanent deformation was confined to the front portion of the projectile. Comparisons of impact force-time histories reveal that higher peak impact forces were associated with shorter impact durations (Fig. 5), reduced projectile displacements.

Figure 3: Gas-gun setup

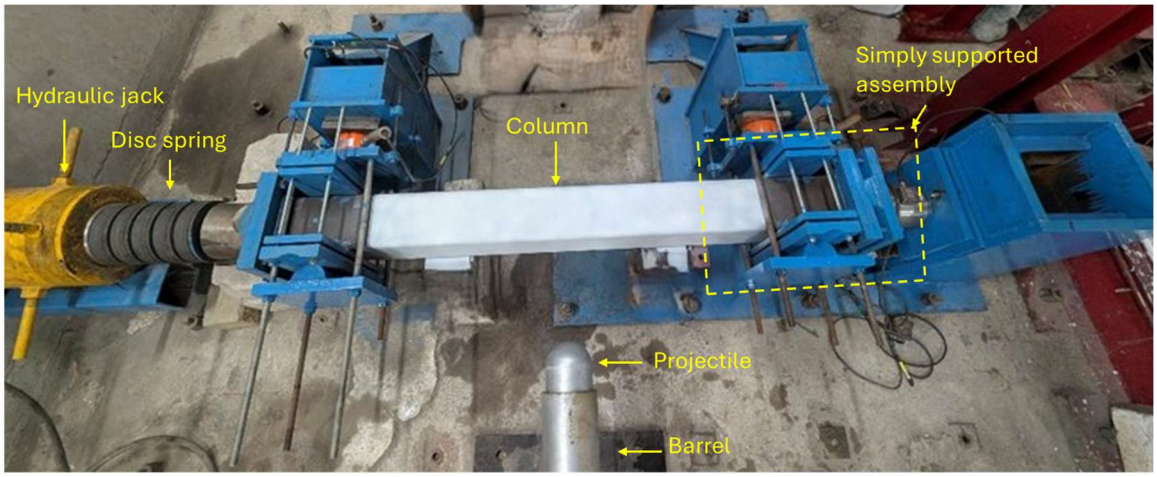

Figure 4: Column mounting setup

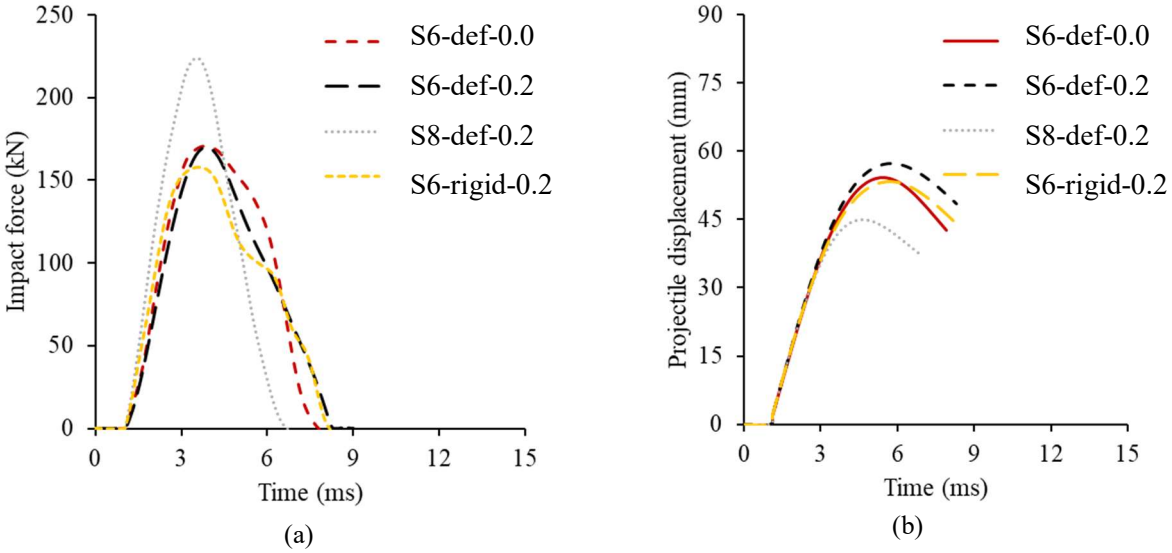

Figure 5: (a) Impact force histories and (b) projectile displacement vs time plot

2.2 Post-impact axial compression tests

Following the lateral impact tests, the residual axial load-carrying capacities of the impacted SHS columns were evaluated using a 12,000 kN capacity CTM. To ensure consistency between the impact and residual compression stages, the specimens were tested under identical boundary conditions. Simply supported end conditions were simulated using concave-convex cylindrical end assemblies that permitted free end rotation while restraining lateral translation. Axial compression tests were conducted under displacement control at a constant loading rate of 1 mm/min. Loading was continued beyond the peak axial resistance until a post-peak load reduction of at least 20% was achieved. Column alignment was carefully ensured prior to testing to minimize unintended eccentricities.

Column deformation and global response were monitored using a 3D DIC system. The residual axial load-carrying capacity obtained from these tests was used to quantify the post-impact residual strength of each specimen. The residual capacity ratio, *CR*, defined as the ratio of residual axial

capacity to the original axial capacity of the column, was computed for all specimens and is summarized in Table 3. Representative damaged shapes of the axially loaded as-built columns and columns tested after lateral impact are shown in Fig. 6.

Table 3: Test results

Specimen	P_{max} (kN)	$\Delta_{m,max}$ (mm)	$\Delta_{proj,max}$ (mm)	d (mm)	Original axial load capacity (kN)	Post-impact residual axial capacity (kN)	CR = residual capacity/ original capacity
S6					1914		
S8					2514		
S6-def-0.0	170.7	9.90	54.25	29.81	1914	1386	0.72
S6-def-0.2	170.1	12.16	57.27	33.10	1914	1258	0.66
S8-def-0.2	223.6	8.14	45.05	19.65	2514	2253	0.90
S6-rigid-0.2	158.2	13.41	53.24	37.78	1914	1208	0.63

Note: P_{max} : peak impact force (obtained by measuring the projectile acceleration and multiplying it by the projectile mass); $\Delta_{m,max}$: peak mid-point displacement in column; $\Delta_{proj,max}$ is peak projectile displacement; d is residual dent depth in column.

(a)Axially loaded as-built columns (b)Post-impact axially loaded columns

Figure 6: Damaged shapes of columns

Preliminary results from the axial residual compression tests show that all impact damaged specimens ultimately failed by inelastic global bending. The residual axial load-carrying capacities were significantly lower than the corresponding as-built axial capacities (between 63% and 90%), accompanied by a noticeable reduction in initial axial stiffness compared to the undamaged columns. The reduction in residual axial capacity was more pronounced for specimens subjected to higher axial preload levels during impact and for columns impacted by rigid projectiles.

3. Numerical Modeling

Finite element simulations were performed using ABAQUS/Explicit to reproduce the lateral impact and subsequent residual axial compression behaviour of the columns (Fig. 7). The steel

columns and deformable projectiles were modelled using (S4R) shell elements, suitable for capturing large deformations and localized denting in thin-walled members. The rigid projectile, end plates and support plates were modelled using C3D10M solid elements. Column ends were connected to end plates using tie constraints to ensure compatible deformation and load transfer. Simply supported boundary conditions consistent with the experiments were imposed using rigid support plates connected to reference points, allowing axial movement and free end rotation while restraining lateral translation. Axial preload was introduced through a linear spring connector attached to one end plate, with stiffness selected to match the equivalent stiffness of the disc spring assembly (17 kN/mm) used in the tests. The prescribed axial force corresponding to the experimental axial load ratio was applied through this connector, ensuring realistic interaction between axial preload and lateral impact.

General contact was adopted to model all interactions. Hard contact was defined in the normal direction for the projectile-column interface, while tangential behavior was modeled using a penalty-based friction formulation with a coefficient of friction of 0.15. Mesh sensitivity studies were conducted on impact force to establish suitable mesh densities.

The simulations were carried out in four sequential steps: axial preloading, lateral impact, unloading, and residual axial compression. All steps were modeled using a dynamic explicit formulation. During the preloading step, the prescribed axial load was applied through the spring connector. The lateral impact was then simulated under simply supported boundary conditions. Following impact, the axial preload and support constraints were released to allow stabilization of the post-impact configuration. In the final step, axial compression was applied under pin-pin conditions to evaluate the post-impact residual axial capacity of the columns.

Geometric imperfections were included in the models to represent initial imperfections. A combined imperfection consisting of a local dimple with a small amplitude and a global imperfection provided the best agreement with the benchmark axial compression tests of the as-built columns. Residual stresses were not included, as their influence on the axial capacity of closed tubular sections is reported to be marginal (Ma et al., 2016; Meng and Gardner 2021; Zhu et al., 2019).

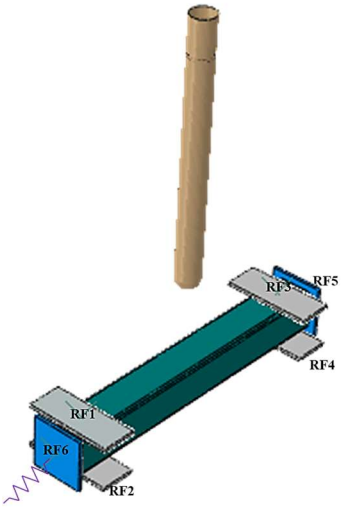

Loading stage	Boundary condition
Axial loading	1. RF1, RF2, RF3, RF4 : Free 2. RF5 : $U_1 = U_2 = U_3 = 0$; $\theta_x \neq \theta_y \neq \theta_z \neq 0$ 3. Pre-axial load applied through the spring
Impact loading	1. RF1, RF2, RF3, RF4 , RF5 : $U_1 = U_2 = U_3 = 0$; $\theta_x \neq \theta_y \neq \theta_z \neq 0$ 2. Axial load propagated
Unloading	1. RF1, RF2, RF3, RF4 : Free 2. RF5 : $U_1 = U_2 = U_3 = 0$; $\theta_x \neq \theta_y \neq \theta_z \neq 0$ 3. 3. Pre-compression removed
Residual axial capacity	1. RF1, RF2, RF3, RF4 : Free 2. RF5 : $U_x = U_y = U_z = 0$; $\theta_x \neq \theta_y \neq \theta_z \neq 0$ 3. RF6 : $U_x = U_y = 0$; $U_z \neq 0$; $\theta_x \neq \theta_y \neq \theta_z \neq 0$

Figure 7: FE model details

Steel exhibits strain-rate-dependent behavior, with strength increasing under high loading rates. To capture this effect in impact simulations, a suitable constitutive model is required. In this study, the Johnson-Cook (JC) model was adopted due to its wide use in dynamic metal deformation and its relatively simple parameterization (Johnson and Cook 1985; Sangani et al. 2024b). The model describes the combined effects of plastic strain, strain rate, and temperature on material strength and is expressed as,

$$\sigma_{plastic} = (A + B\varepsilon^{n})(1 + C\ln(\dot{\varepsilon}^{*}))(1 - (T^{*})^{m}) \quad (1)$$

where ε is the equivalent plastic strain and $\dot{\varepsilon}^{*} = \dot{\varepsilon}/\dot{\varepsilon}_0$ is the normalized strain rate. $\dot{\varepsilon}_0$ is the reference strain rate and T^{*} is the homologous temperature. Johnson-Cook parameters for YSt 310 steel were adopted from high strain-rate material characterization studies reported by Sangani et al. (2024c) and used directly for the column material.

The stress-strain response of EN8 steel showed significantly higher strain hardening compared to YSt 310 steel (Fig. 2), making direct adoption of YSt 310 parameters inappropriate. Therefore, the JC hardening parameters B and n for EN8 steel were calibrated using quasi-static tensile coupon test data, while the strain-rate sensitivity parameter C was assumed to be the same as that of YSt 310 steel due to the absence of high strain-rate test data for EN8. The complete set of Johnson-Cook parameters used in the simulations is summarized in Table 4.

Table 4: JC parameters for column and projectile materials

Material	*A*	*B*	*n*	*C*	*m*
YSt 310	*	334.5	0.462	0.013	1.075
EN8	370.0	1614.2	0.594	0.013	1.075

Note: *Parameter *A* for columns (S6 and S8) was adjusted to match $\sigma_{0.2}$ from coupon tests (Table 1).

3.1 Validation of FE model

The finite element model for SHS columns was validated against experimental results from lateral impact and residual axial compression tests. Key numerical experimental comparisons are summarized in Table 5.

The FE model predicted peak impact forces with good accuracy, with an average FE/Exp ratio of 0.97 (COV = 0.05). The simulated impact force-time histories closely matched the experimental responses, capturing both the initial force rise and subsequent decay due to projectile deformation and column denting (Fig. 8). Projectile displacement and energy absorption were also predicted accurately, with average FE/Exp ratios of 0.94 and 0.97, respectively (COV ≤ 0.05). The numerical displacement-time histories matched the experimental trends, indicating that the main energy dissipation mechanisms were well represented. The FE model further reproduced the axial load response during impact and the post-impact residual axial capacity, with average FE/Exp ratios of 1.03 and 1.02 (COV ≤ 0.05). Overall, the FE simulations show good agreement with the experiments and reliably capture both the impact and post-impact behavior of the SHS columns.

Table 5: Comparisons of FE results with experiment data

Specimen	Max. impact force (kN)			Max. projectile displacement (mm)			Axial load after impact (kN)			Residual axial capacity (kN)		
	Exp	FE	FE/Exp	Exp	FE	FE/Exp	Exp	FE	FE/Exp	Exp	FE	FE/Exp
S6	-	-	-	-	-	-	-	-	-	1915	1891	0.99
S6-def-0.0	170.7	178.3	1.04	54.25	51.73	0.95	-	-	-	1386	1410	1.02
S6-def-0.2	170.1	160.6	0.94	57.27	50.36	0.88	349.2	355.1	1.02	1258	1222	0.97
S8	-	-	-	-	-	-	-	-	-	2514	2708	1.08
S8-def-0.2	223.6	217.2	0.97	45.05	42.47	0.94	475.2	496.1	1.04	2253	2291	1.02
S6-rigid-0.2	158.2	161.0	1.02	53.24	48.73	0.92	353.3	355.5	1.01	1208	1266	1.05
		Average	0.97			0.94			1.03			1.02
		COV	0.05			0.05			0.02			0.05

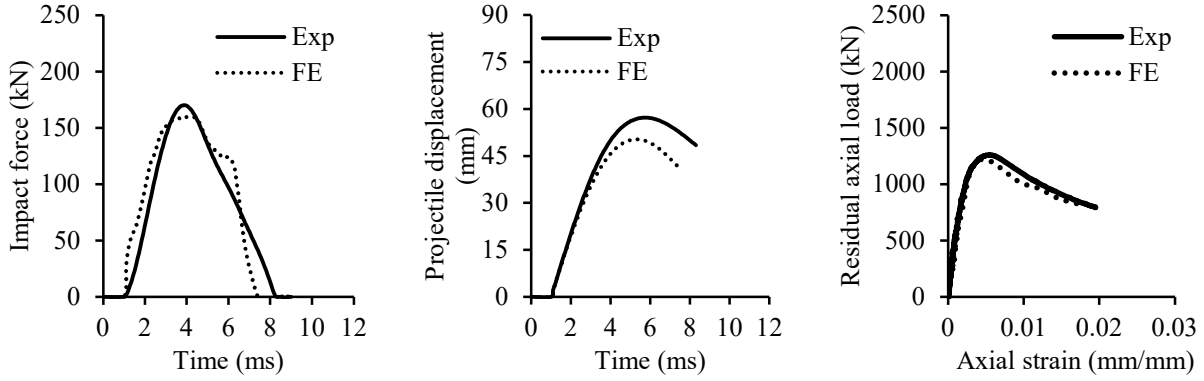

(a)Impact force (b)Projectile displacement (c)Post-impact axial load

Figure 8: Comparison of test and FE data for S6-def-0.2

4. Results and Discussions

The results presented in Table 3 and Fig. 5 demonstrate that both projectile deformability and axial preload significantly influence the impact response and post-impact performance of SHS columns. Rigid projectiles consistently produced more severe localized damage than deformable projectiles, leading to greater stiffness degradation and reduced residual capacity. For specimen S6, rigid projectile impact (S6-rigid-0.2) resulted in approximately a 7% lower peak impact force and a 14% greater residual dent depth compared with deformable projectile impact (S6-def-0.2). These differences were reflected in the residual compression tests, where the axial capacity reduction increased from about 34% for deformable projectiles to approximately 37% for rigid projectiles. Columns impacted by deformable projectiles also exhibited higher initial post-impact axial stiffness. This behavior is attributed to differences in energy transfer mechanisms: rigid projectiles transfer most of the impact energy directly to the column, causing severe localized damage, whereas deformable projectiles dissipate a portion of the energy through their own plastic deformation, thereby limiting damage and preserving residual strength.

Wall thickness was found to have a pronounced effect on both impact resistance and post-impact residual capacity. Increasing the wall thickness from 6 mm (S6-def-0.2) to 8 mm (S8-def-0.2)

increased the peak impact force by approximately 30% and reduced residual dent depth by about 40%. Consequently, the reduction in residual axial capacity decreased markedly from approximately 28% for the 6 mm thick column to about 10% for the 8 mm thick column. The superior performance of thicker sections is primarily attributed to their higher cross-sectional stiffness, which restrains local deformation and limits stiffness degradation during impact.

The axial load ratio also had a significant influence on post-impact behavior. Although increasing axial preload caused only a marginal reduction in peak impact force, it substantially increased local damage and residual capacity degradation. For specimen S6-def-0.2, the residual dent depth increased by approximately 11% compared with the zero-preload case (S6-def-0.0). More importantly, residual compression tests showed that increasing the axial load ratio from 0 to 0.2 increased the reduction in axial capacity from approximately 28% to 34%. This response is governed by the interaction between axial compression and impact-induced bending, where second order (P–Δ) effects intensify global deformation, accelerate stiffness degradation, and reduce post-impact load-carrying capacity.

5. Conclusions

This study investigated the lateral impact response and post-impact residual axial capacity of axially preloaded square hollow section (SHS) steel columns through experiments and finite element simulations. Based on the findings, the following conclusions are drawn:

1. Projectile deformability significantly influences impact damage and residual strength. Rigid projectiles caused greater local damage and stiffness degradation than deformable projectiles, resulting in higher residual dent depths and larger reductions in post-impact axial capacity. Columns impacted by deformable projectiles consistently retained a higher proportion of their original axial capacity.
2. Axial preload increases impact-induced damage and reduces residual capacity. Increasing axial load ratio led to increased local deformation and a pronounced reduction in residual axial strength.
3. Increasing wall thickness improves post-impact performance. Thicker SHS columns exhibited higher impact resistance, reduced local damage, and significantly improved retention of axial load-carrying capacity following impact, demonstrating the effectiveness of increased cross-sectional stiffness in mitigating impact-induced degradation.
4. Impact damage alters the governing failure mode. While as-built SHS columns failed according to their section compactness, all impact-damaged columns failed predominantly by global buckling during residual compression. The impact-induced dent acted as a dominant geometric imperfection, overriding the original section classification.

Acknowledgments

We acknowledge the Prime Minister's Research Fellowship (ID: 2002196), MoE, India, granted to Prithvi Sangani.

References

ASTM E8. 2010. “ASTM E8/E8M standard test methods for tension testing of metallic materials 1.” *Annu. B. ASTM Stand. 4*, (C): 1–27. https://doi.org/10.1520/E0008.

Chen, Y., R. Zhu, C. Zhang, H. Liu, Z. Tu, S. Hu, B. Qiu, and P. Chen. 2025. “Experimental investigation on damage behavior and residual axial capacity of circular steel tube for offshore wind turbine jacket foundation subjected

to lateral impact." *Constr. Build. Mater.*, 489 (June): 142310. Elsevier Ltd. https://doi.org/10.1016/j.conbuildmat.2025.142310.

Cui, G., X. Zhai, and L. Meng. 2023. "Behavior of axially loaded high-strength steel circular hollow section tubes under low velocity lateral impact." *Thin-Walled Struct.*, 185 (January): 110595. Elsevier Ltd. https://doi.org/10.1016/j.tws.2023.110595.

Johnson, G. R., and W. H. Cook. 1985. "Fracture characteristics of three metals subjected to various strains, strain rates, temperatures and pressures." *Eng. Fract. Mech.*, 21 (1): 31–48. https://doi.org/10.1016/0013-7944(85)90052-9.

Li, W., Y. Z. Gu, L. H. Han, X. L. Zhao, R. Wang, M. Nassirnia, and A. Heidarpour. 2019. "Behaviour of ultra-high strength steel hollow tubes subjected to low velocity lateral impact: Experiment and finite element analysis." *Thin-Walled Struct.*, 134 (January 2018): 524–536. Elsevier Ltd. https://doi.org/10.1016/j.tws.2018.10.026.

Ma, J.-L., T.-M. Chan, and B. Young. 2016. "Experimental Investigation on Stub-Column Behavior of Cold-Formed High-Strength Steel Tubular Sections." *J. Struct. Eng.*, 142 (5): 04015174. https://doi.org/10.1061/(asce)st.1943-541x.0001456.

Meng, X., and L. Gardner. 2021. "Testing, modelling and design of normal and high strength steel tubular beam-columns." *J. Constr. Steel Res.*, 183: 106735. Elsevier Ltd. https://doi.org/10.1016/j.jcsr.2021.106735.

Sangani, P., and A. Agarwal. 2024. "A comprehensive methodology for residual capacity evaluation of damaged steel tubular columns." *J. Constr. Steel Res.*, 216 (March): 108625. Elsevier Ltd. https://doi.org/10.1016/j.jcsr.2024.108625.

Sangani, P., K. Ghoshal, and A. Agarwal. 2025. "Behavior of Hollow Steel Tubular Columns Subjected to Low-Velocity Lateral Impact by Deformable Projectile: Numerical Studies BT - Safeguarding Structural Resilience Under Extreme Events." K. H. Tan, N. Banthia, V. Kodur, Y.-X. Ma, and S. Soleimani-Dashtaki, eds., 447–456. Cham: Springer Nature Switzerland.

Sangani, P., D. Kumar, S. N. Khaderi, K. Ghoshal, and A. Agarwal. 2024a. "Numerical Analysis of Low-Velocity Deformable Projectile Impact on Steel Columns BT - Recent Developments in Structural Engineering, Volume 1." M. D. Goel, R. Kumar, and S. S. Gadve, eds., 601–609. Singapore: Springer Nature Singapore.

Sangani, P., D. Kumar, I. Paliwal, M. Ramji, S. N. Khaderi, and A. Agarwal. 2024b. "Material properties of YSt 310 steel tubular columns under extreme loading conditions." *J. Constr. Steel Res.*, 223 (June): 109076. Elsevier Ltd. https://doi.org/10.1016/j.jcsr.2024.109076.

Sangani, P., S. Singh, and A. Agarwal. 2023. "Residual strength estimation of damaged steel tubular columns using digital image correlation." *Mater. Today Proc.*, 108 (November 2023): 99–103. Elsevier Ltd. https://doi.org/10.1016/j.matpr.2023.11.049.

Sangani, P., S. Singh, and A. Agarwal. 2024c. "A Comprehensive Approach for Estimating Residual Capacity of Damaged Steel Tubular Sections: From Surface Scanning to Stress Analysis." *Proc. Annu. Stab. Conf. Struct. Stab. Res. Counc. SSRC 2024*.

Wardenier, J. 2011. *Hollow Sections In Structural Applications*. *2nd Ed. CIDECT,Geneva*. Geneva: 2nd Edition, CIDECT.

Zeinoddini, M., G. A. R. Parke, and J. E. Harding. 2002. "Axially pre-loaded steel tubes subjected to lateral impacts: An experimental study." *Int. J. Impact Eng.*, 27 (6): 669–690. https://doi.org/10.1016/S0734-743X(01)00157-9.

Zhu, J. Y., T. M. Chan, and B. Young. 2019. "Cross-sectional capacity of octagonal tubular steel stub columns under uniaxial compression." *Eng. Struct.*, 184 (January): 480–494. Elsevier. https://doi.org/10.1016/j.engstruct.2019.01.066.